ORIGINAL RESEARCH ARTICLE

Microstructure and Wide Temperature Range Tribological Properties of CoCrFeNiTi High-Entropy Alloy Coating by Laser Cladding

Hao Liu, Qiansheng Xu, Linwei Wang ⓘ, Peijian Chen, Xinhua Liu, Qiang Gao, Jingbin Hao, and Haifeng Yang

In order to improve the service life of AISI 4340 steel at high temperatures, CoCrFeNiTi high-entropy alloy (HEA) coating was prepared on AISI 4340 steel by laser cladding in this study. The microstructure and microhardness of this HEA coating are examined, along with its tribological properties and wear mechanisms from 20 to 800 °C. The results reveal that while the primary phase of the CoCrFeNiTi HEA coating is an FCC phase, segregation of Ti elements precipitates a Laves phase with an HCP lattice structure and a χ phase with an α-Mn structure. The average microhardness of the HEA coating is as high as 700 HV0.3, attributed to the solid solution strengthening due to large atomic radius Ti and second-phase strengthening. Given its high hardness, the HEA coating has a low wear rate at room temperature (4.80×10^{-5} mm^3/(N·m)), with adhesive wear being its principal wear mechanism. Yet, at 200 °C, peeling off hard phases changes its wear mechanism to abrasive wear, leading to an increased wear rate of 26.21×10^{-5} mm^3/(N·m). Between 400 and 800 °C, oxidation wear becomes dominant due to high temperatures promoting oxide film formation. At 800 °C, the HEA coating exhibits excellent wear resistance (7.34×10^{-5} mm^3/(N·m)), resulting from dense oxide layers and excellent high-temperature mechanical properties of Laves phase and χ phase.

1. Introduction

AISI 4340 steel is classified as ultra-strength steel, finding extensive application in the production of critical components within the automotive and aerospace industries. This popularity stems from its commendable attributes, including robust toughness, desirable tempering stability, splendid resistance to both fatigue and creep, as documented in previous studies (Ref 1). Nevertheless, its inherent deficiency in wear resistance, particularly under high-temperature conditions, constrains its utility in dynamic components (Ref 2). Hence, surface modification treatments have been employed as a means to enhance the steel's wear resistance, thereby extending its service life at elevated temperatures.

Laser cladding emerges as a highly promising technique for surface modification, distinguished by its advantageous features encompassing high energy density, rapid cooling rates, and minimal thermal impact on the underlying substrate (Ref 3). These inherent benefits not only ensure the desired coating quality but also foster the formation of densely bonded metallurgical layers connecting the coating and substrate (Ref 4). The versatility of laser cladding encompasses a vast array of materials, yet recent attention has converged significantly upon high-entropy alloys (HEAs) due to their exceptional properties. HEAs are typically comprised of 5 to 13 constituent elements, each contributing in a molar ratio ranging from 5% and 35% (Ref 5, 6).This unique compositional design imparts high-entropy alloys with a host of advantageous effect, including high-entropy effect (Ref 7, 8), sluggish diffusion kinetics (Ref 6), lattice distortion effects (Ref 9), and the cocktail effect (Ref 10, 11). Collectively, these attributes culminate in a material exhibiting superior mechanical characteristics (Ref 12), exceptional thermal stability (Ref 13, 14), outstanding wear resistance (Ref 15, 16), and superb corrosion resistance (Ref 17).

CoCrFeNi-based alloys, serving as a representative system of HEAs, have been extensively researched to date. CoCrFeNi HEA, characterized by equiatomic ratios, manifests as a single-phase solid solution with a Face-Centered Cubic (FCC) crystal structure, showcasing outstanding toughness and exceptional damage tolerance. High hardness and excellent wear resistance at RT and high temperatures of this HEA results from the synergistic effects of second-phase strengthening and solid solution strengthening. Yang et al. (Ref 18) conducted laser cladding experiments, depositing FeCoCrNiCux ($x = 0, 0.5, 1$)

Hao Liu and Qiansheng Xu, School of Mechanical and Electrical Engineering, China University of Mining and Technology, Xuzhou, People's Republic of China; and State Key Laboratory of Solid Lubrication, Lanzhou Institute of Chemical Physics, Chinese Academy of Sciences, Lanzhou, People's Republic of China; Linwei Wang, College of Mechanical and Electronic Engineering, Shanghai Jian Qiao University, Shanghai, People's Republic of China; Peijian Chen, School of Mechanics and Civil Engineering, China University of Mining and Technology, Xuzhou, People's Republic of China; Xinhua Liu, Qiang Gao, Jingbin Hao, and Haifeng Yang, School of Mechanical and Electrical Engineering, China University of Mining and Technology, Xuzhou, People's Republic of China. Contact e-mail: wanglinwei@gench.edu.cn.

HEA coatings onto SU304 substrates. Their finding indicated that the addition of Cu increased the lattice distortion of the FCC solid solution, enhancing the ductility and work-hardening ability of the coatings. This improvement led to increased wear resistance of FeCoCrNiCux HEA coatings at RT. At 600 °C, the presence of Cu element resulted in the formation of a dense oxide film, preventing direct contact between the counterparts and the coating, thereby effectively reducing the coefficient of friction and wear rate. Wu et al. (Ref [19]) prepared CoCrFeNi/ WC composite coatings with a WC content ranging from 0 to 40 wt.% by laser cladding. They discovered that grain refinement and second-phase particle strengthening due to WC contributed to the hardness and wear resistance of the coatings. However, when the WC content increased to 40 wt.%, the coatings became severely embrittled, leading to a decrease in wear resistance. In a parallel study, Liu et al. (Ref [20]) prepared CoCrFeMnNi HEA coatings with varying Ti contents by laser cladding. Notably, the CoCrFeMnNiTi$_{0.25}$ coatings retained a singular FCC solid solution phase, while an increase in Ti content promoted the precipitation of intermetallic compounds Fe$_2$Ti within the coating. The combination of solid solution strengthening and second-phase strengthening in these coatings led to a substantial surge in microhardness and a notable reduction in wear loss. Furthermore, the incorporation of carbon and silicon in FeCoCrNi-based HEAs has been shown to improve the mechanical properties and enhance wear resistance (Ref [21-23]). Nevertheless, it is crucial to acknowledge that laser cladding inevitably incurs burning and blow-off losses of Si and C elements due to their low melting point and low density. The alloying of Cu is detrimental to the hardness of the coating, while the addition of particles is prone to cracking.

In the context of this research, titanium (Ti) was selected as the alloying element for the CoCrFeNi HEA coating. Prior investigations indicated that CoCrFeNiTi HEA coatings hold promise for applications in high-temperature environments, owing to the presence of Laves phases and other intermetallic compounds (Ref [24, 25]). However, the influence of temperature on the dry wear behavior of CoCrFeNiTi HEA coating in a wide temperature range remains unclear. Consequently, CoCrFeNiTi HEA coating was prepared on AISI 4340 steel substrate in this study, and a comprehensive examination of the microstructure and tribological properties at elevated temperature was undertaken. This research not only contributes to extending the service life of AISI 4340 steel alloy but also provides a theoretical basis for utilization of CoCrFeNiTi HEA coatings in high-temperature environments.

2. Materials and Methods

For this study, the annealed AISI 4340 steel alloy, with dimensions of 100 mm × 100 mm × 10 mm, was selected as the substrate material. The chemical composition of the AISI 4340 steel substrate is presented in Table 1. The cladding powder is a mixture of high purity (≥ 99.5 wt.% in purity) Co, Cr, Fe, Ni, and Ti powders with particle size ranging from 45 to 150 μm. Prior to the laser cladding process, the powder was dried in a vacuum at 100 °C for 8 hours to ensure optimal fluidity. The laser cladding was executed utilizing a YLS400-CTTC-Y11 fiber laser, equipped with a DPSF-2 powder feeder, while high-purity argon gas was used as the protective gas. To prevent fracture initiation, a WXD-SERIES thermostatic heater was employed to maintain the substrate temperature consistently above 200 °C throughout the experimentation. The processing parameters for the laser cladding are meticulously detailed in Table 1.

The prepared CoCrFeNiTi HEA coating was sectioned into specimens measuring 15 mm × 15 mm × 10 mm using a DK7745 wire-cutting machine. Subsequently, these specimens underwent grinding and polishing to facilitate metallographic observations. An x-ray diffractometer (XRD, the Bruker D8 Advanced) with Cu-K radiation and a scanning speed of 2°/min was used to identify the phase constitution of the coating. The microstructure was investigated by scanning electron microscopy (SEM, FEI Quanta 250) with energy disperse spectroscopy (EDS). Transmission electron microscopy (TEM, JEM-2100) with selected area electron diffraction (SAED) is used to characterize the phase structures of the coating further.

The microhardness of the coating was assessed using a Vickers hardness tester (Huayin HVSA-1000A), with testing parameters set to a 3 N load and a 15 s dwell time. The tribological properties of the coating, ranging from room temperature(RT) to 800 °C, were evaluated utilizing a pin-on-disk friction and wear tester (HT-1000). The Si$_3$N$_4$ ceramic was selected as the friction pair due to its high hardness (1700 HV) and low roughness (Ra = 0.2 μm), ensuring stability throughout the experimental process. The experimental conditions included a load of 2 N, a friction radius of 4 mm, a rotating speed of 600 rpm·min^{-1}, and test temperatures set at 20 °C, 200 °C, 400 °C, 600 °C, and 800 °C. The total wear time was maintained at 30 min. To examine the worn surface of the coatings, SEM and EDS were employed. The wear resistance of the CoCrFeNiTi HEA coating was calculated based on the volume wear rate, determined by the following formula:

$$W = \frac{V}{FL} \qquad \text{(Eq 1)}$$

where W represents the volume wear rate, V denotes the volume loss of the coating, F signifies the experimental load, and L is the sliding length.

3. Results and Discussion

Figure 1 displays the XRD pattern of the CoCrFeNiTi HEA coating. As observed, the coating exhibits diffraction peaks corresponding to three distinct phases. The primary diffraction

Table 1 Chemical composition of AISI 4340 steel

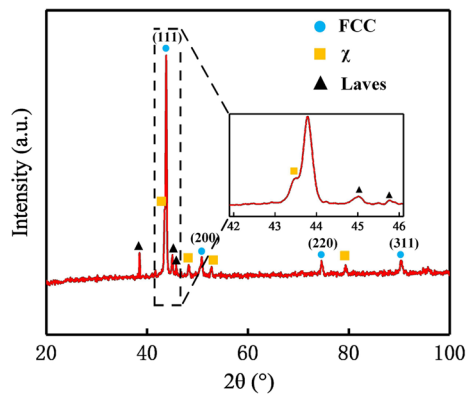| Element	Fe	C	Si	Mn	Cr	Ni	Mo	P	S
Wt.%	Balance	0.37-0.44	0.17-0.37	0.50-0.80	0.60-0.90	1.25-1.75	0.15-0.25	≤ 0.04	≤ 0.04

Fig. 1 XRD pattern of the CoCrFeNiTi HEA coating prepared by laser cladding

peak has the typical FCC lattice structure and is remarkably consistent with the Fe-Ni solid solution phase (JCPDS 47-1417). Specifically, the diffraction angle (2θ) corresponding to the primary FCC phase peak measures 43.494°, with the calculated lattice constant at 0.359 nm. Comparatively, in contrast to the lattice constant of 0.357 nm for CoCrFeNi (Ref 26), the solid solution phase within the CoCrFeNiTi HEA coating experiences expansion-induced distortion. This expansion is attributed to the introduction of Ti elements, which possesses a large atomic diameter and consequently lead to the increase in the lattice constant.

Furthermore, upon closer examination of the XRD pattern, the remaining diffraction peaks are identified as the χ phase with an α-Mn structure (JCPDS 16-0443) and the Laves phase characterized by a close-packed hexagonal structure. It is worth noting that the diffraction peaks corresponding to the Laves phase do not precisely match to any standard Powder Diffraction File (PDF) cards. In general, the unique nature of the laser cladding process as well as the inherent high-entropy effect of HEAs can inhibit the formation of intermetallic compounds. However, Ti differs significantly from other elements, notably in terms of atomic radius and electronegativity, making it prone to segregation within the coating. Moreover, Ti exhibits a substantial negative mixing enthalpy when interacting with Co, Cr, Fe, or Ni ($- 28$, $- 7$, $- 17$, and $- 35$ kJ/mol, respectively). Consequently, segregated Ti is highly susceptible to combining with other elements during the solidification process, ultimately resulting in the precipitation of intermetallic compounds. As a consequence, the laser cladding of the CoCrFeNiTi coating predisposes it to the formation of both the χ phase and the Laves phase.

The cross-sectional microstructure morphologies of the CoCrFeNiTi HEA coating are visually presented in Fig. 2. As depicted in Fig. 2(a), the CoCrFeNiTi coating has an approximate thickness of 3.2 mm, with a calculated coating dilution rate of 11.1%. Notably, it is devoid of any discernible pores or cracks. Figure 2(b) shows the morphologies of the bonding area. As observed, due to the inhomogeneous microstructure of the as-cast AISI 4340 steel, black spots appear below the bonding area after etching. Plane crystals with a thickness of about 10 μm are prominently evident above the bonding area, while columnar dendrite crystals extend in the direction opposite to the heat flow above these plane crystals. This sequence of microstructure morphologies from the bonding interface to the uppermost portion of the coating follows a

consistent pattern of transitioning through planar crystals, columnar dendrite crystals, and equiaxed dendrites. The underlying cause of this phenomenon is closely associated to the temperature gradient-to-solidification rate ratio, denoted as G/R in the laser cladding process. In proximity to the bonding interface, G/R attains exceedingly high value, thereby facilitating the growth of plane crystals. As the distance to the bonding interface becomes larger, the G/R ratio diminishes, combining with a shift in the direction of heat dissipation. Consequently, this change in conditions leads to the emergence of columnar dendrite crystals and eventually equiaxed dendrites (Ref 27).

The enlarged view in Fig. 2(c-d) shows the microstructure is composed of the dendritic region (DR), light gray interdendritic region (IR), and black petal-like precipitation (P). The EDS mapping and spot results of the coating, as shown in Fig. 3 and Table 2, reveal that elemental Ti is slightly segregated in the IR and significantly enriched within the P phase. Based on the XRD results, it can be inferred that the P phase is an AB$_2$-type Laves phases.

According to the microstructure morphologies of the CoCrFeNiTi HEA coating depicted in Fig. 2(c-d), the DR is considered a matrix phase with an FCC lattice structure, while the IR is a Ti-rich χ phase. This is further demonstrated by the elemental composition of the DR and IR, as shown in Table 2. The χ phase is prone to being generated in iron-based alloys with high Cr, Mo, and Ti elemental composition and has also been reported in HEAs (Ref 28). Furthermore, the χ phase is distributed in the IR, which is related to its relatively low precipitation temperature and the limited solid solution of Ti elements in the FCC phase. Chen et al. (Ref 29) investigated the precipitation behavior of the χ phase by aging it at 600-1050 °C for 24 hours. The χ phase precipitates at 600-900 °C and dissolves above 1000 °C. The melting point of the FCC phase in CoCrFeNi HEA is above 1200 °C [30]. During solidification, dendrites rich in Co, Cr, Fe, and Ni are the first to solidify. Concurrently, due to its larger atomic radius, Ti becomes enriched in the mushy region adjacent to the dendrites, setting the stage for the nucleation of the Laves phase. As cooling proceeds, the remaining Ti elements segregate between the dendrites, creating favorable conditions for the precipitation of the χ phase. Additionally, similar to other additive manufacturing technologies (Ref 31), the complex thermal cycle history of laser cladding provides another means for precipitating the χ phase.

Figure 4(a) shows typical bright-field morphologies of the CoCrFeNiTi HEA coating. As depicted in Fig. 4(a), three phases are present, consistent with the SEM and XRD results. It is noteworthy that the elemental Ti content in the Laves phase is low and does not correspond to the AB$_2$ chemical formula. This discrepancy could be attributed to the complex elemental composition, which expands the solubility range of the Laves phase. Thoma et al. (Ref 32) demonstrated that when Ti is added to NbCr$_2$, the Ti atom can replace both Nb and Cr atoms, thereby expanding the room temperature solubility range of the Laves phase from 2 to 4 at.%. In this study, the Laves phase comprises five elements: Co, Cr, Fe, Ni, and Ti. The intricate elemental composition broadens the solubility range of the Laves phase. Additionally, laser cladding is a typical non-equilibrium solidification process, causing the elemental composition of the Laves phase to deviate from the equilibrium region. The interplay of these two factors results in a lower than expected Ti content in the Laves phase. Furthermore, compo-
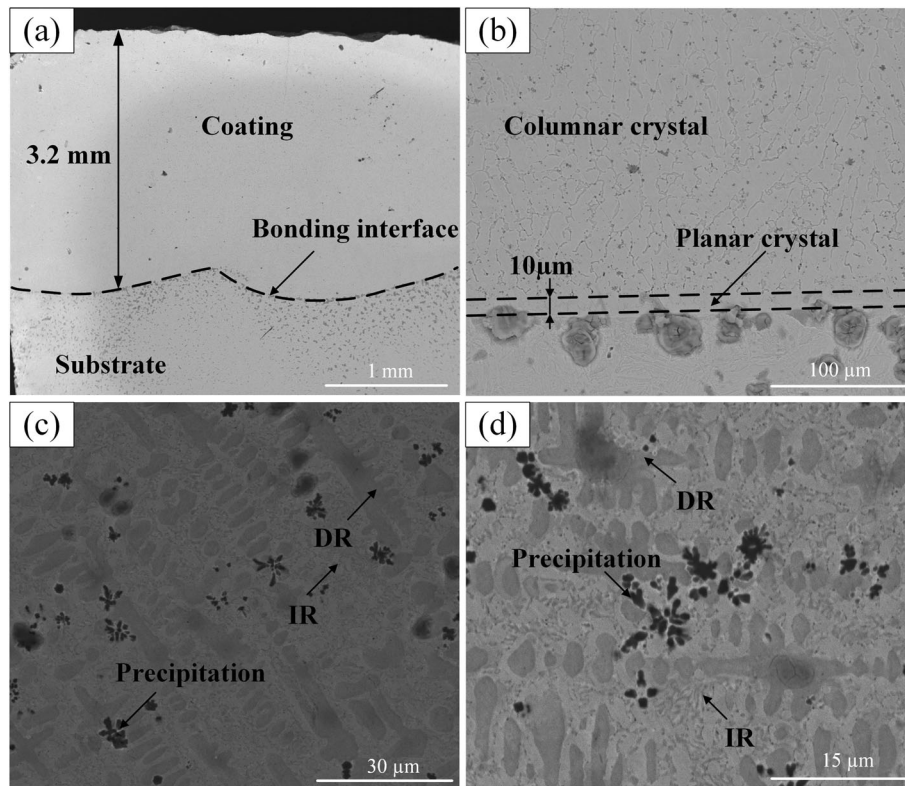
Fig. 2 Cross-sectional microstructure morphologies of CoCrFeNiTi HEA coating: (a) low magnification image outlines overall microstructure; (b) bonding zone; (c) cladding zone and (d) a high magnification image of the outlined cladding zone in (c)
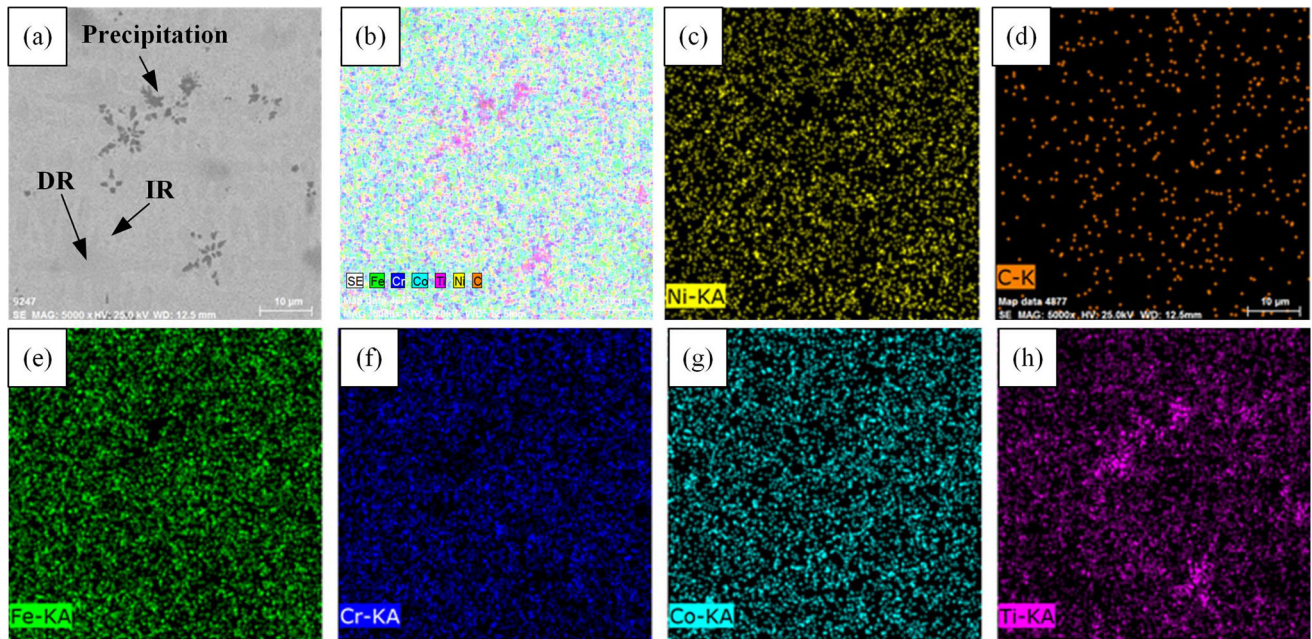

Fig. 3 (a–h) EDS mapping results for CoCrFeNiTi HEA coating

sitional variations and complex elemental compositions in the Laves phase may also account for the discrepancy between the diffraction peaks of the Laves phase and the standard powder diffraction file card. When the elemental composition of the Laves phase deviates from the chemical ratios of AB₂, the excess atoms may occupy their own or other atoms' positions,

leading to constitutional vacancies or anti-site substitution (Ref 32, 33). By comparing the elemental composition of the Laves phase in Fig. 4a, it can be determined that the excess atoms are small-sized B atoms such as Fe, Cr, Ni, and Cr. Excessive small-sized atoms may occupy the positions of large sized atoms, resulting in anti-site substitution and an increase in the

lattice constant (Ref 34). On the other hand, the complexity of atom types in the Laves phase could further increase the lattice distortion, altering to the lattice constant. The combination of these two factors may cause the diffraction peak position of the Laves phase to deviate from the standard powder diffraction card.

The selected area electron diffraction (SAED) patterns of these phases are shown in Fig. 4(b), (c), and (d). According to the high magnification images and SAED patterns in Fig. 4(b-d), the presence of Fe-Ni solid solution phases with an FCC lattice structure, χ phases with an α-Mn structure, and Laves phase is confirmed. The EDS results show that there are only a few (approximately 11 at.%) Ti elements in the FCC phase, demonstrating the limited solubility of the Ti element.

Interestingly, a large number of parallel streamlines are found in the Laves phase at the junction with the matrix phase, as shown in Fig. 5. At the same time, the distinct streaks at the diffraction points in the corresponding regions indicate that

they are high-density stacking faults (SFs). Li et al. (Ref 35) demonstrated that SFs or twin faults could formed in the Laves phase at a lower energy cost than conventional dislocation slip, and the high lattice distortion energy also favors the formation of SFs, corresponding to the lattice distortion effect of HEAs.

Figure 6 shows the microhardness distribution curve of the CoCrFeNiTi HEA coating along the depth direction. The microhardness curve reveals three distinct regions, namely the coating region, the heat-affected zone (HAZ), and the substrate. Notably, the microhardness of the coating fluctuates, whereas the microhardness of both the substrate and the HAZ remains relatively stable. It is a well-established fact that laser cladding fosters a good metallurgical bond between the coating and the substrate. However, it is inevitable that the distribution of

Table 2   Processing parameters for laser cladding

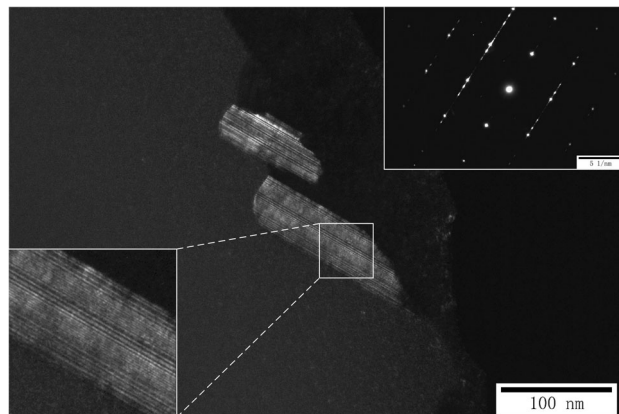| Process parameter	Value
Power (W)	1800
Spot diameter (mm)	4
Scanning speed (mm/s)	5
Defocusing distance (mm)	+ 30
Overlap rate (%)	60
Powder feeding speed (g/min)	9.4
Protective gas flow (L/min)	3

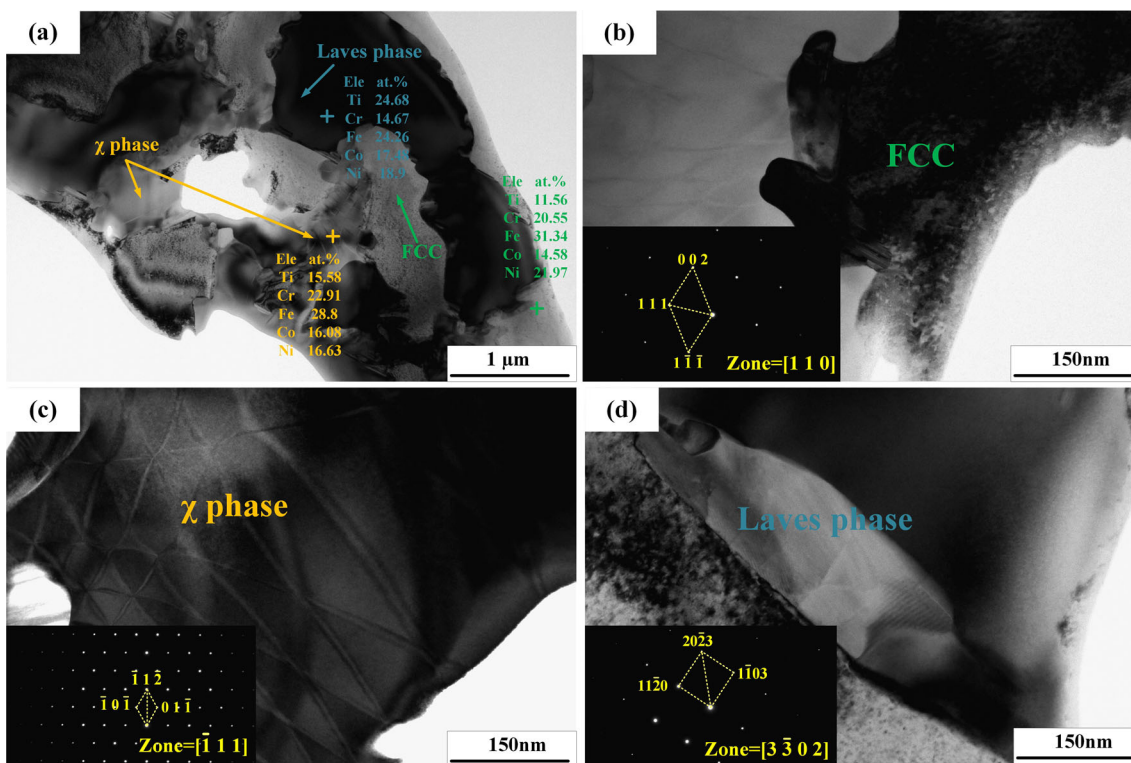**Fig. 5**   The dark-field image of Laves phases with SFs

Fig. 4   TEM morphologies and SAED results of CoCrFeNiTi HEA coating: (a) low magnification TEM image, (b) FCC phase, (c) χ phase, and (d) Laves phase

elements within the coating is affected by the constituents of the substrate, commonly referred to as the dilution effect. As a consequence of the dilution effect, the bottom portion of the
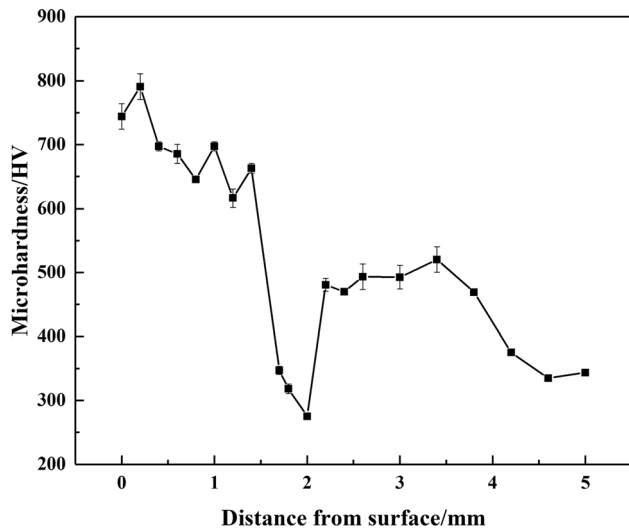

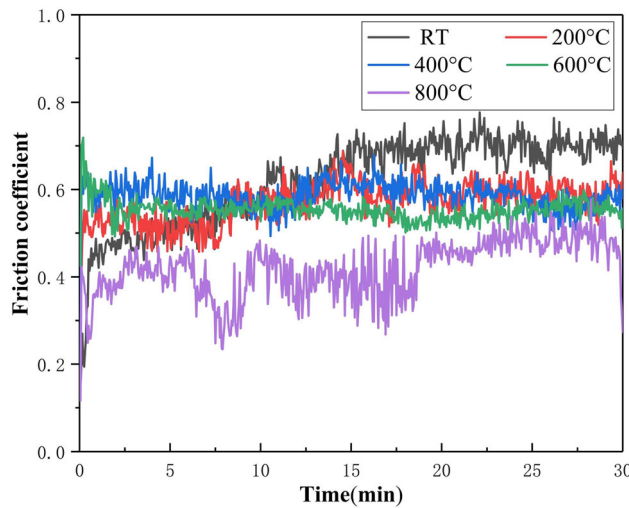**Fig. 6** Microhardness distribution along the depth direction of the CoCrFeNiTi HEA coating

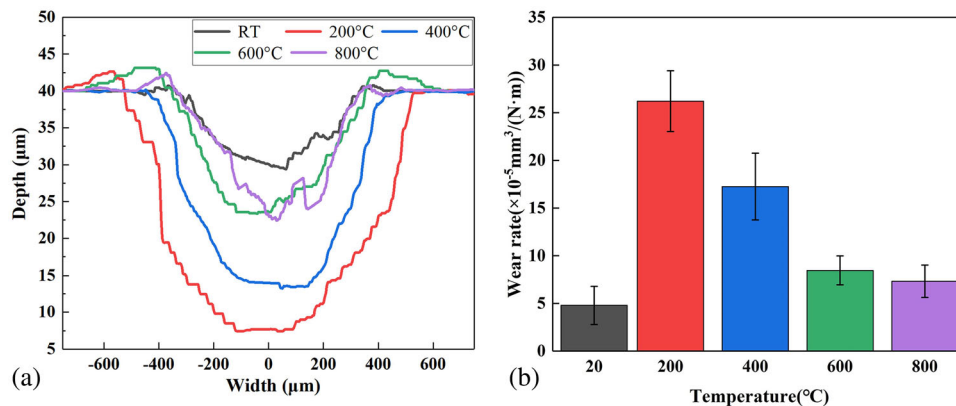**Fig. 7** Coefficient of friction curves at different temperatures

coating tends to introduce higher concentrations of iron (Fe) elements. Importantly, Fe serves as a stabilizer for the FCC phase (Ref 36), effectively augmenting the volume fraction of the FCC phase. This, in turn, leads to a decrease in the microhardness. Besides, the fluctuations in microhardness within the coating may also be related to the inhomogeneous distribution of precipitates. Notably, the average microhardness of AISI 4340 steel and the heat-affected zone are 320 HV0.3 and 505 HV0.3, respectively. Conversely, the average micro-hardness of the coating attains the highest value, measuring 700 HV0.3. This translates to an approximate 2.18-fold increase in microhardness compared to that of the substrate.

Figure 7 shows the friction coefficient curves of CoCrFe-NiTi at different temperatures. The average coefficients of friction at RT, 200 °C, 400 °C, 600 °C, and 800 °C are 0.619, 0.570, 0.586, 0.554, and 0.420, respectively. At RT, there is a noticeable running-in stage, with the coefficient of friction rising over time and then stabilizing around 0.7. However, there is no apparent running-in stage at high temperatures. This is due to the high contact stress of the asperities of the friction pair in the running-in stage, which causes severe wear and, therefore, a significant increase in the friction coefficient (Ref 20). In contrast, there is no significant running-in phase at elevated temperatures, which could be related to the reduction of contact stress with the softening of the asperities. At 200-600 °C, the rotational sliding process is relatively stable, and the friction coefficient ranges from 0.5 to 0.6. However, the coefficient of friction exhibits significant fluctuation in the dry sliding test at 800 °C and finally stabilizes at about 0.45. It can be observed that temperature significantly affects the friction of CoCrFeNiTi HEA coating, meaning that the coefficient of friction decreases with increasing temperature. This is probably not only because the resistance of the coating to plastic deformation decreases, but also because of the change in the wear mechanism caused by rising temperature. In addition, all friction coefficient curves exhibit a sawtooth phenomenon, due to the periodic accumulation and elimination of abrasive debris and periodic local fracture of the wear surface (Ref 37).

Figure 8 shows the two-dimensional profile of the wear surface and wear rates at different temperatures. It can be observed that the depth and width of the wear marks of the coating at RT are the smallest (309 μm and 737 μm, respectively), and the wear rate is calculated to be 4.80×10^{-5} mm^3/(N·m). However, the wear marks of the coating at 200 °C are the largest (867 μm and 1094 μm, respectively), with the worst

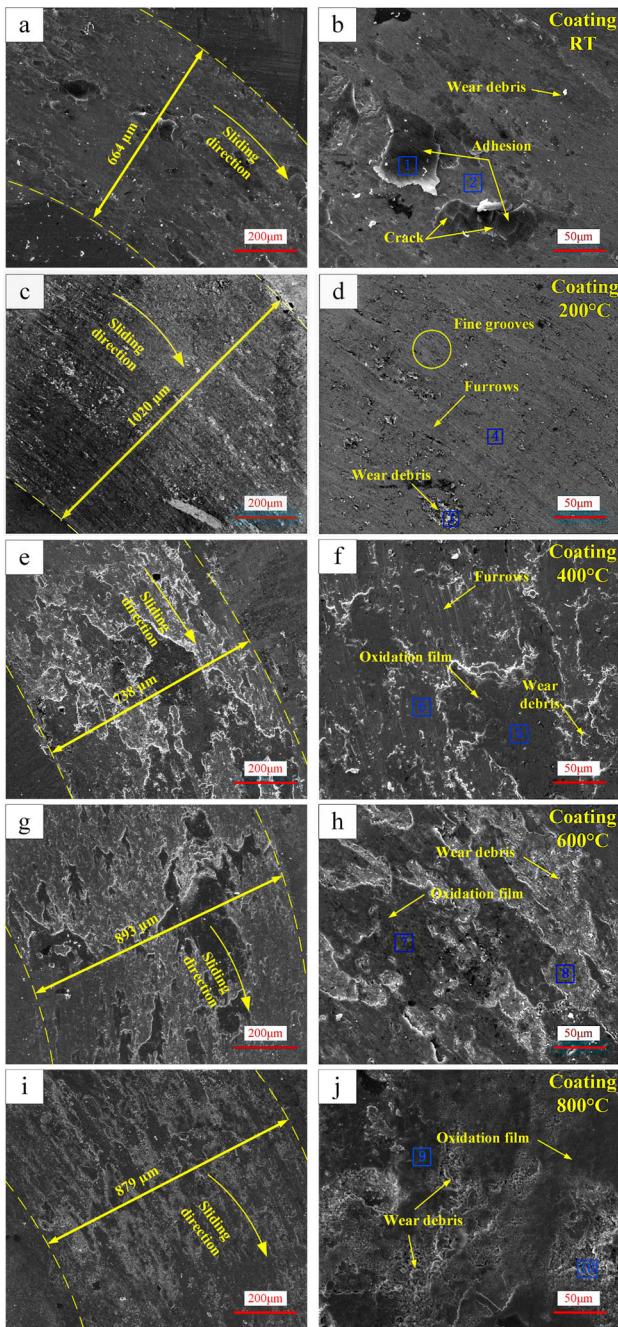**Fig. 8** Wear profiles (a) and volume wear rate (b) of CoCrFeNiTi coating at different temperatures

Fig. 9 Wear surface morphologies of CoCrFeNiTi HEA coating at RT (a, b), 200 °C (c, d), 400 °C (e, f), 600 °C (g, h), and 800 °C (i, j)

wear resistance (26.21 × 10⁻⁵ mm³/(N·m)). This may indicate a significant change in the wear mechanism of the coating at 200 °C. With further increases in temperature, the wear rates of the coating decrease. The depth of the coating wear mark at 600 °C is 539 μm, and the width is 818 μm, which is not significantly different from that at 800 °C. In summary, the wear rate of the HEA coating shows a trend of increasing and then decreasing with increasing temperature. The wear rate of the coating is 7.34 × 10⁻⁵ mm³/(N·m) at 800 °C, demonstrating good wear resistance at elevated temperatures.

The morphology and EDS results of the wear surface at different temperatures are shown in Fig. 9 and Table 3. As depicted in Fig. 9(a) and (b), the wear marks at RT are rough, with plastic deformation, adhesion and wear debris, indicating an adhesive wear mechanism. Since the hardness of Si_3N_4 balls is much higher than that of the wear surface, adhesive wear mainly occurs on the coating. The EDS results (point 1 and 2) show a high elemental oxygen content in the adhesion layer, resulting from the oxidation reaction induced by the frictional heat of the dry sliding process. The oxidation reaction enhances the brittleness of the adhesions, promoting the initiation and expansion of microcracks on the adhesion and eventually leading to the peeling of the adhesion along the cracks. Furthermore, the coating has the highest Si content in the abrasion marks at RT, suggesting the most severe material transfer. Adhesive wear involves atomic bonding between the asperities of the friction pair, meaning that the friction force is large. As a result, the coefficient of friction is largest at RT under the same load. According to Archard's law (Ref 38), the wear rate of the coating is inversely proportional to its hardness. Herein, the high hardness of CoCrFeNiTi HEA at RT is responsible for its low wear rate.

As shown in Fig. 9(c) and (d), the wear mark is smoother at 200 °C and has a width of about 1020 μm. The wear surface has furrows with wear debris and slight plastic deformation on both sides, suggesting that the wear mechanism of the coating transforms from adhesive to abrasive wear. The oxygen concentration of the wear surface and wear debris is reduced at 200 °C compared to RT, as shown by the EDS data for point 3 and 4 in Table 4, implying a higher material removal efficiency. There are also many fine grooves on the wear surface, indicating microcutting is an important means of material removal for CoCrFeNiTi HEA coating during dry sliding tests at 200 °C. However, as temperature increases, the

Table 3 The EDS spot results of different phases for CoCrFeNiTi HEA coating.

EDS spot	Chemical composition (at.%)				
	Co	Cr	Fe	Ni	Ti
DR	17.92	24.82	33.84	14.26	9.17
IR	18.08	22.63	28.60	12.61	18.08
Precipitation	12.61	17.65	23.96	11.52	34.25

Table 4 EDS spot results for CoCrFeNiTi HEA coating wear marks

EDS spot	Chemical composition (at.%)						
	O	Fe	Co	Cr	Ni	Ti	Si
1	53.81	11.06	8.34	6.74	8.13	10.43	1.49
2	29.68	20.52	12.24	14.44	9.64	12.28	1.20
3	45.12	16.73	9.77	10.21	8.83	9.29	0.05
4	11.19	28.09	15.71	15.45	15.20	13.74	0.63
5	57.43	14.08	5.75	8.13	7.42	7.08	0.11
6	14.82	27.51	11.91	17.61	14.10	13.81	0.24
7	62.64	10.52	7.24	6.90	6.85	5.70	0.15
8	36.27	17.34	11.50	9.22	9.87	15.40	0.41
9	64.46	11.91	6.16	5.86	5.44	5.67	0.49
10	68.62	10.14	5.47	5.20	4.80	5.50	0.27

FCC phase is more likely to soften, producing uncoordinated strain between the matrix phase and second phases in the plastic deformation region. This results in these hard phases being more likely to break and peel off, and act as abrasive particle between the friction pairs. This is why the wear mechanism changes to abrasive wear at 200 °C.

The wear mark morphologies of CoCrFeNiTi HEA coating at 400 °C and 600 °C are similar, covering some oxide particles and oxide layers, as shown in Fig. 9(e)-(h). The oxide film is formed by the oxidation and compaction of wear debris under high temperatures and normal load, preventing direct contact between the coating and the counterpart and protecting the coating from wear. At 400 °C, a few furrows are discovered in the region where the oxide film is not covered, indicating that the coating tested at 400 °C involves oxidation wear and slight abrasive wear. The EDS results also reveals that the wear surface and the oxide film contain more oxygen as the temperature rises. It means the oxide film is more fully oxidized at higher temperatures. Moreover, there are no furrows in the wear area, so the wear mechanism of the coating at 600 °C is oxidation wear.

The coverage area of the oxide film on the wear mark at 800 °C is the largest, as shown in Fig. 9(i) and (j), and the content of elemental oxygen is highest (point 9 and 10), indicating that the wear mechanism at 800 °C is severe oxidative wear. The high hardness of the oxide film provides an excellent protective effect as well as a friction reduction effect on the wear surface. As a result, the coating has a low friction coefficient and good wear resistance at 800 °C. Moreover, the sharp fluctuations in the friction coefficient curve at 800 °C are also related to the oxide film. In the initial phase, the wear surface is covered with thin and brittle oxide layers. As the dry sliding test progresses, the brittle oxide layer breaks down, causing fluctuations in the coefficient of friction. The broken oxide layer also acts as three-body abrasive particles, further increasing the friction coefficient fluctuations. This process also occurs at 400 °C and 600 °C, but the oxidation is most severe at 800 °C, resulting in the largest fluctuations in friction coefficient. With further oxidation, three-body abrasive particles develop into compacted layers (thicker, more stable oxide film) under normal load, and then the friction coefficient curve becomes stable. Additionally, Laves phase and χ phase can maintain high hardness at elevated temperatures. According to the results obtained from Westbrook (Ref 39), hardness of the χ phase in the Fe-Cr-Mo system at RT and 800 °C is 1000 HV and 440 HV, respectively. High hardness of the χ phase and Laves phase, especially at high temperatures, could contribute to the improvement in the wear resistance of the coating over a wide temperature range. This is another crucial reason for the excellent wear resistance of CoCrFeNiTi HEA coating at elevated temperatures.

In addition, to discern the types of oxides formed, the Gibbs free energy of various oxidation reactions involving elements in the CoCrFeNiTi HEA reacting with oxygen are shown in Fig. 10. From the results, all considered oxide oxidation reactions can proceed spontaneously, and the curves with positive slopes indicate the stability of the oxides is strengthened with the increase in temperature (Ref 18). Among the secondary reactions that yield products such as $CoCr_2O_4$, $NiCr_2O_4$, Co_2TiO_4, and $CoTiO_3$, the Gibbs free energies are larger, making these reactions less likely to occur. Thus, it can be inferred that the oxides on the wear scar are primarily produced by the direct reaction between the metal and oxygen.
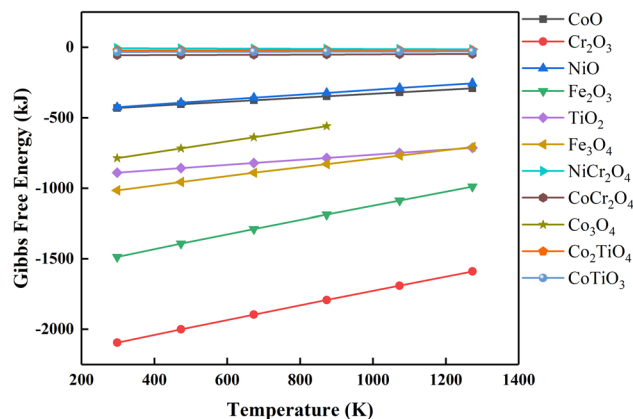

Fig. 10 Gibbs free energy for oxidation reactions

Table 5 The R_{P-B} values of metal oxides on wear surface

Metal oxide	CoO	Cr_2O_3	NiO	Fe_2O_3	Fe_3O_4	TiO_2
R_{P-B}	1.74	2.02	1.70	2.15	2.10	1.76

It can be also noted that the Gibbs free energy of the oxidation reaction of Co, Ni, and Ti elements is smaller, making it more difficult for these elements to be oxidized on the wear scar. Conversely, Fe and Cr elements are more prone to oxidation, leading to the production of oxides. Combined with the EDS results presented in Table 4, it can be observed that the content of Fe and Cr elements in the oxide film is higher at RT-400 °C, while the content of oxygen elements is lower, suggesting that the oxidation may not be fully carried out. Therefore, it is presumed that the oxide film at RT-400 °C is primarily composed of Cr_2O_3 and Fe_2O_3, with a lesser content of oxides such as TiO_2, Co_3O_4, and NiO, and possibly some incomplete oxides, such as Fe_3O_4 and FeO At 600-800 °C, the content of oxygen element in the oxide film is higher, and apart from the higher content of Fe element due to the dilution effect, the content of Co, Ni, Ti, and Cr elements is nearly uniform, indicating that the oxidation reaction is fully carried out in this temperature range. Therefore, it is inferred that at 600-800 °C, the oxide film consists of fully oxidized oxides such as Cr_2O_3, Fe_2O_3, TiO_2, CoO, and NiO, with a higher content of Fe_2O_3 due to dilution effects.

In order to investigate the effect of different oxides on the wear behavior, the Pilling–Bedworth ratio (R_{P-B}) was introduced as an index for evaluating the protective ability of the oxide film [40]. The calculation formula is listed as follows:

$$R_{P-B} = \frac{V_{oxide}}{n \cdot V_{metal}} = \frac{M_{oxide} \cdot \rho_{metal}}{n \cdot M_{metal} \cdot \rho_{oxide}} \quad \text{(Eq 2)}$$

where the R_{P-B} formula represents the volume ratio between the metal oxide films and the consumed metal, M is the relative atomic or molecular mass, n is the number of metal atoms contained in each oxide molecule, ρ is the density, and V stands for the molar volume. The R_{P-B} values of the oxides that could be present in the oxide film are shown in Table 5. When the R_{P-B} value is between 1 and 2, the oxide film gets good protection, such as NiO and TiO_2. When the R_{P-B} value is larger than 2, the oxides are loose with high expansion rates, promoting the
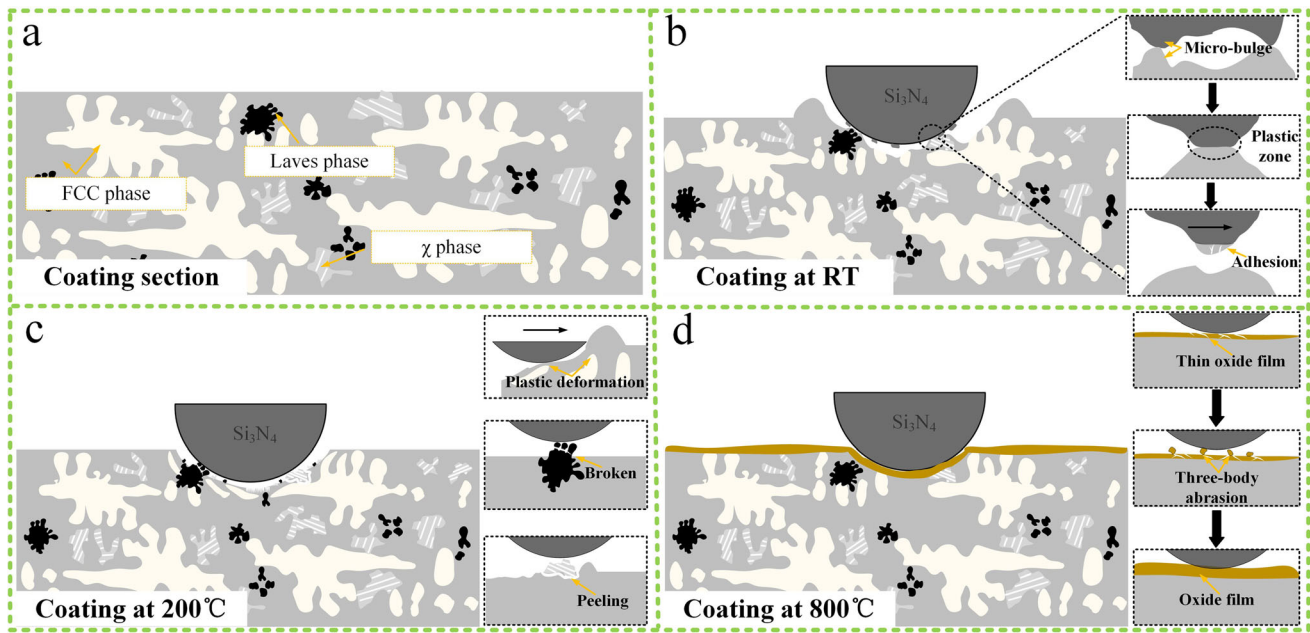
Fig. 11 Schematic illustration of the microstructure (a) and wear mechanisms at RT (b), 200 °C (c), and 800 °C (d) for CoCrFeNiTi HEA coating

formation of cracks, such as Fe_2O_3, Fe_3O_4, and Cr_2O_3. At RT RT-400 °C, the oxide is mainly composed of Cr_2O_3 and Fe_2O_3 which are brittle. This is the reason that the oxide film appears cracks. In this case, the oxide is not only poorly protective, but also easily broken into debris that microcut the surface of the coating. At 600-800 °C, Fe and Cr elements are preferentially oxidized at the beginning of the experiment, producing a thin and brittle oxide film. As the wear continues, the content of oxides with good protective effect such as NiO, TiO_2, and CoO increases. These oxides form a dense oxide film under repeated rolling of the counterparts, leading to enhance the tribological properties of the coating at high temperatures.

Figure 11 presents a schematic illustration of the microstructure and wear mechanism at various temperatures for the CoCrFeNiTi HEA coating. The study revealed that the CoCrFeNiTi HEA coating, prepared by laser cladding, is dense and comprises the FCC phase, χ phase, and Laves phase. Owing to the strengthening effect of the second phase, the CoCrFeNiTi HEA coating exhibits high hardness. However, the shedding of the hard phase results in a transition in the wear mechanism of the coating from adhesive wear at RT to abrasive wear at 200 °C. With a further increase in temperature, oxidation wear progressively becomes the dominant wear mechanism, and the coating displays excellent tribological properties at 800 °C. This study lends support to the high-temperature application of CoCrFeNiTi HEA.

4. Conclusion

In the present work, the microstructure and tribological behavior of CoCrFeNiTi HEA coating prepared by laser cladding were investigated over a wide temperature range. The main phase of the CoCrFeNiTi HEA coating is a single-phase solid solution with an FCC lattice structure. However, due to the limited solid solution of Ti elements in the FCC phase, the Ti-rich Laves phase and χ phase are precipitated. Owing to the second-phase strengthening and solid solution strengthening, the CoCrFeNiTi HEA coating achieves a high microhardness of 700 HV0.3. This high microhardness endows the coating with excellent wear resistance, and its wear mechanism is mainly adhesive wear. However, due to the softening of the primary FCC solid solution at 200 °C, the wear rate rises to its highest value of 26.21×10^{-5} mm^3/(N·m). The wear mechanism and tribological properties of CoCrFeNiTi HEA coating are critically dependent on temperature, with abrasive wear evolving to oxidation wear as the temperature increases. As a result, the wear rate of the coating decreases to 7.34×10^{-5} mm^3/(N·m), exhibiting desirable tribological properties at 800 °C.

References

1. N. Saeidi and A. Ekrami, Comparison of Mechanical Properties of Martensite/Ferrite and Bainite/Ferrite Dual Phase 4340 Steels, *J. Mater. Sci. Eng. A-Struct. Mater. Prop. Microstruct. Process.*, 2009, **523**(1–2), p 125–129. https://doi.org/10.1016/j.msea.2009.06.057
2. H. Zhong, L. Dai, Y. Yue, B. Wang, X. Zhang, C. Tan, M. Ma, and R. Liu, Tribological Properties of Plasma-Nitrided AISI 4340 Steel in

Vacuum, *J. Mater. Sci. Technol. Mater. Sci. Technol.*, 2016, **32**(4), p 275–281. https://doi.org/10.1080/02670836.2015.1121341

3. S. Sun, Y. Durandet, and M. Brandt, Parametric Investigation of Pulsed Nd: YAG Laser Cladding of Stellite 6 on Stainless Steel, *J. Surf. Coat. Technol.*, 2005, **194**(2–3), p 225–231. https://doi.org/10.1016/j.surfcoat.2004.03.058

4. Y. Zhang, J. Li, Y.Q. Jiang, D.N. Kang, Y.F. Juan, and Z.J. Lu, Investigation Into Corrosion and Wear Behaviors of Laser-Clad Coatings on Ti6Al4V, *J. Mater. Res. Express*, 2020, **7**(1), p 016587. https://doi.org/10.1088/2053-1591/ab6a53

5. B. Cantor, I.-T. Chang, P. Knight, and A.-J. Vincent, Microstructural Development in Equiatomic Multicomponent Alloys, *J. Mater. Sci. Eng. A-Struct. Mater. Prop. Microstruct. Process.*, 2004, **375**, p 213–218. https://doi.org/10.1016/j.msea.2003.10.257

6. J.W. Yeh, S.K. Chen, S.J. Lin, T.S. Chin, T.T. Shun, C.H. Tsau, and S.Y. Chang, Nanostructured High-Entropy Alloys with Multiple Principal Elements: Novel Alloy Design Concepts and Outcomes, *J. Adv. Eng. Mater.*, 2004, **6**(5), p 299–303. https://doi.org/10.1002/adem.200300567

7. T.M. Yue, H. Xie, X. Lin, H.O. Yang, and G.H. Meng, Solidification Behaviour in Laser Cladding of AlCoCrCuFeNi High-Entropy Alloy on Magnesium Substrates, *J. J. Alloy. Compd.*, 2014, **587**, p 588–593. https://doi.org/10.1016/j.jallcom.2013.10.254

8. X. Yang and Y. Zhang, Prediction of High-Entropy Stabilized Solid-Solution in Multi-Component Alloys, *J. Mater. Chem. Phys.*, 2012, **132**(2–3), p 233–238. https://doi.org/10.1016/j.matchemphys.2011.11.021

9. Y. Zhang, Y.J. Zhou, J.P. Lin, G.L. Chen, and P.K. Liaw, Solid-Solution Phase Formation Rules for Multi-component Alloys, *J. Adv. Eng. Mater.*, 2008, **10**(6), p 534–538. https://doi.org/10.1002/adem.200700240

10. J.W. Yeh, Recent Progress in High-Entropy Alloys, *J. Ann. Chim.-Sci. Mat.*, 2006, **31**(6), p 633–648. https://doi.org/10.4028/www.scientific.net/AMR.631-632.227

11. S. Ranganathan, Alloyed Pleasures: Multimetallic Cocktails, *J. Curr. Sci.*, 2003, **85**(10), p 1404–1406

12. C. Wang, T.H. Li, Y.C. Liao, C.L. Li, J.S. Jang, and C.H. Hsueh, Hardness and Strength Enhancements of CoCrFeMnNi High-Entropy Alloy with Nd Doping, *J. Mater. Sci. Eng. A-Struct. Mater. Prop. Microstruct. Process.*, 2019, **764**, p 138192. https://doi.org/10.1016/j.msea.2019.138192

13. C. Huang, Y.Z. Zhang, J.Y. Shen, and R. Vilar, Thermal Stability and Oxidation Resistance of Laser Clad TiVCrAlSi High Entropy Alloy Coatings on Ti-6A1-4V Alloy, *J. Surf. Coat. Technol.*, 2011, **206**(6), p 1389–1395. https://doi.org/10.1016/j.surfcoat.2011.08.063

14. H. Liu, J. Liu, X. Li, P.J. Chen, H.F. Yang, and J.B. Hao, Effect of Heat Treatment on Phase Stability and Wear Behavior of Laser Clad AlCoCrFeNiTi$_{0.8}$ High-Entropy Alloy Coatings, *J. Surf. Coat. Technol.*, 2020 https://doi.org/10.1016/j.surfcoat.2020.125758

15. L. Yang, Z. Cheng, W.W. Zhu, C.C. Zhao, and F.Z. Ren, Significant Reduction in Friction and Wear of a High-Entropy Alloy via the Formation of Self-organized Nanolayered Structure, *J. J. Mater. Sci. Technol.*, 2021, **73**, p 1–8. https://doi.org/10.1016/j.jmst.2020.08.065

16. L.M. Du, L.W. Lan, S. Zhu, H.J. Yang, X.H. Shi, P.K. Liaw, and J.W. Qiao, Effects of Temperature on the Tribological Behavior of Al$_{02.5}$CoCrFeNi High-Entropy Alloy, *J. J. Mater. Sci. Technol.*, 2019, **35**(5), p 917–925. https://doi.org/10.1016/j.jmst.2018.11.023

17. J.L. Lv, T.X. Liang, C. Wang, and L.M. Dong, Effect of Ultrafine Grain on Tensile Behaviour and Corrosion Resistance of the Duplex Stainless Steel, *J. Mater. Sci. Eng. C-Mater. Biol. Appl.*, 2016, **62**, p 558–563. https://doi.org/10.1016/j.msec.2016.02.008

18. C.M. Yang, X.B. Liu, Y.F. Liu, Z.X. Zhu, Y. Meng, H.B. Zhou, and S.H. Zheng, Effect of Cu-Doping on Tribological Properties of Laser-Cladded FeCoCrNiCux High-Entropy Alloy Coatings, *J. Tribol. Int.*, 2023, **188**, p 108868. https://doi.org/10.1016/j.triboint.2023.108868

19. T. Wu, Y.X. Chen, B. Lin, L.T. Yu, W.Y. Gui, J.H. Li, Y. Wu, and D.W. Zeng, Effects of WC on the Microstructure, Wear and Corrosion Resistance of Laser-Deposited CoCrFeNi High Entropy Alloy Coatings, *J. Coatings*, 2022, **12**(7), p 985. https://doi.org/10.3390/coatings12070985

20. P.F. Liu, W.D. Si, D.B. Zhang, S.C. Dai, B.C. Jiang, D. Shu, L.L. Wu, C. Zhang, and M.S. Zhang, Microstructure and Friction Properties of CoCrFeMnNiTix High-Entropy Alloy Coating by Laser Cladding, *J. Mater.*, 2022, **15**(13), p 4669. https://doi.org/10.3390/ma15134669

21. L. Guo, X.Q. Ou, S. Ni, Y. Liu, and M. Song, Effects of Carbon on the Microstructures and Mechanical Properties of FeCoCrNiMn High Entropy Alloys, *J. Mater. Sci. Eng. A-Struct. Mater. Prop. Microstruct. Process.*, 2019, **746**, p 356–362. https://doi.org/10.1016/j.msea.2019.01.050

22. H. Liu, J. Liu, P.J. Chen, and H.L. Yang, Microstructure and High Temperature Wear Behaviour of in-situ TiC Reinforced AlCoCrFeNi-Based High-Entropy Alloy Composite Coatings Fabricated by Laser Cladding, *J. Opt. Laser Technol.*, 2019, **118**(10), p 140–150. https://doi.org/10.1016/j.optlastec.2019.05.006

23. Z.X. Zhu, X.B. Liu, Y.F. Liu, S.Y. Zhang, Y. Meng, H.B. Zhou, and S.H. Zhang, Effects of Cu/Si on the Microstructure and Tribological Properties of FeCoCrNi High Entropy Alloy Coating by Laser Cladding, *J. Wear.*, 2023, **512**, p 204533. https://doi.org/10.1016/j.wear.2022.204533

24. S.Y. Zhang, B. Han, M.Y. Li, Q. Zhang, C.Y. Hu, S.Y. Niu, Z.H. Li, and Y. Wang, Investigation on Solid Particles Erosion Resistance of Laser Cladded CoCrFeNiTi High Entropy Alloy Coating, *J. Intermetallics*, 2021, **131**, p 107111. https://doi.org/10.1016/j.intermet.2021.107111

25. Y.Z. Li, Y.B. Hu, D.Z. Zhang, and W.L. Cong, Laser Remelting of CoCrFeNiTi High Entropy Alloy Coatings Fabricated by Directed Energy Deposition: Effects of Remelting Laser Power, *J. Opt. Laser Technol.*, 2023, **158**, p 108871. https://doi.org/10.1016/j.optlastec.2022.108871

26. Y. Qiu, S. Thomas, D. Fabijanic, A.J. Barlow, H.L. Fraser, and N. Birbilis, Microstructural Evolution, Electrochemical and Corrosion Properties of AlxCoCrFeNiTiy High Entropy Alloys, *J. Mater. Des.*, 2019, **170**, p 107698. https://doi.org/10.1016/j.matdes.2019.107698

27. J.C. Lippold, *Welding Metallurgy and Weldability*, Hoboken, John Wiley Sons, 2014, p 132. https://doi.org/10.1002/9781118960332

28. B. Gwalani, A.V. Ayyagari, D. Choudhuri, T. Scharf, S. Mukherjee, M. Gibson, and R. Banerjee, Microstructure and Wear Resistance of an Intermetallic-Based Al$_{0.25}$Ti$_{0.75}$CoCrFeNi High Entropy Alloy, *J. Mater. Chem. Phys.*, 2018, **210**, p 197–206. https://doi.org/10.1016/j.matchemphys.2017.06.034

29. S.H. Chen, T. Liang, Y.T. Zhou, W.W. Xin, C.W. Zheng, Y.C. Ma, J.M. Wu, G.B. Li, and K. Liu, Phase Characterization and Formation Behavior in 6 wt% Si High-silicon Austenitic Stainless Steel During Isothermal Aging, *J. Acta Metall. Sin. Engl. Lett.*, 2021, **34**(5), p 649–656. https://doi.org/10.1007/s40195-020-01152-7

30. J.B. Zhang, X. Li, Y.C. Zhang, F. Zhang, H.X. Wu, X.Z. Wang, Q. Zhou, and H.F. Wang, Sluggish Dendrite Growth in an Undercooled High Entropy Alloy, *J. Intermet.*, 2020, **119**, p 106714. https://doi.org/10.1016/j.intermet.2020.106714

31. C.Y. Bai, L. Lan, R.Y. Xin, S. Gao, and B. He, Microstructure Evolution and Cyclic Deformation Behavior of Ti-6Al-4 V Alloy via Electron Beam Melting During Low Cycle Fatigue, *J. Int. J. Fatigue*, 2022, **159**, p 106784. https://doi.org/10.1016/j.ijfatigue.2022.106784.32

32. D.J. Thoma and J.H. Perepezko, A geometric analysis of solubility ranges in Laves phases, *J. J. Alloy. Compd.*, 1995, **224**(2), p 330–341. https://doi.org/10.1016/0925-8388(95)01557-4

33. D.J. Thoma, F. Chu, P. Peralta, P.G. Kotula, K.C. Chen, and T.E. Mitchell, Elastic and Mechanical Properties of Nb (Cr, V)$_2$C$_{15}$ Laves Phases, *J. Mater. Sci. Eng. A-Struct. Mater. Prop. Microstruct. Process.*, 1997, **239**, p 251–259. https://doi.org/10.1016/j.msea.2019.01.050

34. J.H. Zhu, L.M. Pike, C.T. Liu, and P.K. Liaw, Point Defects in Binary Laves Phase Alloys, *J. Acta Mater.*, 1999, **47**(7), p 2003–2018. https://doi.org/10.1016/S1359-6454(99)00090-7

35. M. Li, Z.H. Zhang, A.S. Thind, G.D. Ren, R. Mishra, and K. Flores, Microstructure and Properties of NbVZr Refractory Complex Concentrated Alloys, *J. Acta Mater.*, 2021, **213**, p 116919. https://doi.org/10.1016/j.actamat.2021.116919

36. G. Anis, M.M. Attallah, M. Youssef, and H. Salem, Temperature-Dependent Enthalpy and Entropy Stabilization of Solid Solution Phases in Non-equiatomic CoCrFeNiTi High Entropy Alloys: Computational Phase Diagrams and Thermodynamics, *J. Model. Simul. Mater. Sci. Eng.*, 2022, **30**(4), p 045013. https://doi.org/10.1088/1361-651X/ac6687

37. J.M. Wu, S.J. Lin, J.W. Yeh, S.K. Chen, and Y.S. Huang, Adhesive Wear Behavior of AlxCoCrCuFeNi High-Entropy Alloys as a Function of Aluminum Content, *J. Wear*, 2006, **261**(5–6), p 513–519. https://doi.org/10.1016/j.wear.2005.12.008

38. J.F. Archard, Contact and Rubbing of Flat Surfaces, *J. J. Appl. Phys.*, 1953, **24**(8), p 981–988. https://doi.org/10.1063/1.1721448

39. J.H. Westbrook, Temperature Dependence of the Hardness of Secondary Phases Common in Turbine Bucket Alloys, *J. JOM*, 2017, **9**, p 898–904. https://doi.org/10.1007/BF03397938

40. K. Annand, M. Nord, I. Maclaren, and M. Gass, The Corrosion of $Zr(Fe, Cr)_2$ and Zr_2Fe Secondary Phase Particles in Zircaloy-4 Under 350 °C Pressurised Water Conditions, *J. Corrosion Sci.*, 2017, **128**, p 213–223. https://doi.org/10.1016/j.corsci.2017.09.014